

PCCP

Accepted Manuscript



This is an *Accepted Manuscript*, which has been through the Royal Society of Chemistry peer review process and has been accepted for publication.

Accepted Manuscripts are published online shortly after acceptance, before technical editing, formatting and proof reading. Using this free service, authors can make their results available to the community, in citable form, before we publish the edited article. We will replace this *Accepted Manuscript* with the edited and formatted *Advance Article* as soon as it is available.

You can find more information about *Accepted Manuscripts* in the [Information for Authors](#).

Please note that technical editing may introduce minor changes to the text and/or graphics, which may alter content. The journal's standard [Terms & Conditions](#) and the [Ethical guidelines](#) still apply. In no event shall the Royal Society of Chemistry be held responsible for any errors or omissions in this *Accepted Manuscript* or any consequences arising from the use of any information it contains.

ARTICLE

Modulating Light Propagation in ZnO-Cu₂O-Inverse Opal Solar Cell for Enhanced Photocurrents

Cite this: DOI: 10.1039/x0xx00000x

Natalia Yantara^a, Thi Thu Trang Pham^a, Pablo P. Boix^b, Nripan Mathews^{a,b*}Received 00th April 2015,
Accepted 00th January 2012

DOI: 10.1039/x0xx00000x

www.rsc.org/

The advantages of using an interconnected periodic ZnO morphology, i.e. an inverse opal structure, on electrodeposited ZnO/Cu₂O devices are presented. The solar cells are fabricated by low cost solution based methods such as spin coating and electrodeposition. The impact of inverse opal geometry, mainly the diameter and thickness, are scrutinized. By employing 3 layers of inverse opal structure with 300nm pore diameters, higher short circuit photocurrents (~84% improvement) are observed, however the open circuit voltages reduce with increasing interfacial area. Optical simulation using finite difference time domain method shows that the inverse opal structure modulates light propagation within the devices such that more photons are absorbed close to the ZnO/Cu₂O junction. This increases the collection probability resulting in improved short circuit currents.

A. Introduction

Air stable solar cells that employ abundant, non-toxic, and low cost material are attractive in the photovoltaic devices field (e.g. all oxide semiconductor solar cells). Various semiconducting metal oxides such as TiO₂, ZnO, and Cu₂O have been widely studied for photovoltaic applications¹⁻⁵. Cuprous oxide (Cu₂O), which possesses intrinsic p-type semiconducting properties⁶ is of interest as its theoretical maximum power conversion efficiency (PCE) based on Shockley-Queisser limit reaches 20%⁷. Despite the high theoretical PCE limit, the PCE record for photovoltaic devices that employ Cu₂O is only 6.1%⁸. In this case, Na doped thermally oxidized Cu₂O (at ~1010°C) and pulsed laser deposited (Ga_{0.975}Al_{0.025})₂O₃ film were used as p-type and n-type layers respectively. The Na doping increases the carrier concentration while maintaining high mobility (> 100 cm².V⁻¹.s⁻¹). Substituting (Ga_{0.975}Al_{0.025})₂O₃ with ZnO reduced the efficiency to 4.13% accompanied by a loss of open circuit voltage due to more defect levels at the interface⁵. In spite of the superior performance of the thermally oxidized Cu₂O, the high thermal budget will considerably boost the fabrication cost and reduce the attractiveness of the solar cell configuration. Alternatively, other low temperature deposition methods such as electrodeposition⁹⁻¹³ have also been explored, with a record efficiency of 2.65%¹⁴. Room temperature electrodeposited Cu₂O and atomic layer deposited ZnO were employed as the p-type and n-type semiconducting material. Although electrodeposited Cu₂O devices have a wide depletion region (approximately 2.7µm), recombination within the depletion layer plays a significant role in governing the device efficiency. The electron drift length within the depletion region (L_{drift}) of Cu₂O varies with the quality of Cu₂O film. Electrodeposited Cu₂O devices give lower efficiency in comparison to thermally oxidised layers due to their shorter L_{drift}¹⁵. As the drift length of

the photo-generated electrons and holes (~110nm) is shorter than the Cu₂O optical absorption depth (~500nm at λ= 500nm), there is a reduction of the incident photon to current efficiency (IPCE) of electrodeposited Cu₂O devices for wavelengths above 500nm. To address this problem, extending the electron collection material into the Cu₂O film by using nanorods have been previously explored¹⁶⁻¹⁸. Other techniques to confine long wavelength photon inside the Cu₂O film, such as using high haze ZnO film⁴ and incorporating organic buffer layer¹⁹, had also been proven able to enhance the photocurrent.

One such possibility is using inverse opal (IO) architecture to confine the photon inside the absorber material. IO structures could be fabricated by electrodeposition within the polystyrene photonic crystal (PC) template²⁰⁻²⁶. Higher short circuit current which leads to better performances in were observed when larger In₂O₃ IO pore size was used as photoanode in dye sensitized solar cell²⁷. TiO₂ IO structures with pore diameters of 309nm and 394nm have also been successfully employed for quantum dot sensitized CdSe solar cells where their open and interconnected ordered porous structure provided a better infiltration for Cd and Se precursors during the chemical bath deposition which resulted in a uniform coverage of CdSe quantum dots clusters throughout the entire inverse opal layer²⁰. In addition, the periodic change in the dielectric constant of the material could also change the photon density distribution and increase the optical path due to interfacial scattering^{22,25,27}. These kinds of interfacial scattering could provide a solution to the mismatch of the optical absorption depth and the charge drift lengths. Though IO structures have been employed on ZnO/Cu₂O film before, however effect of ZnO IO structure on the solar cell performances was not explored²⁸. Thus it would be interesting to pursue the inverse opal structure in the context of a Cu₂O/ZnO solar cell where a ZnO IO can act as a host for Cu₂O infiltration and study the impact of IO structure geometry on the solar cell performance.

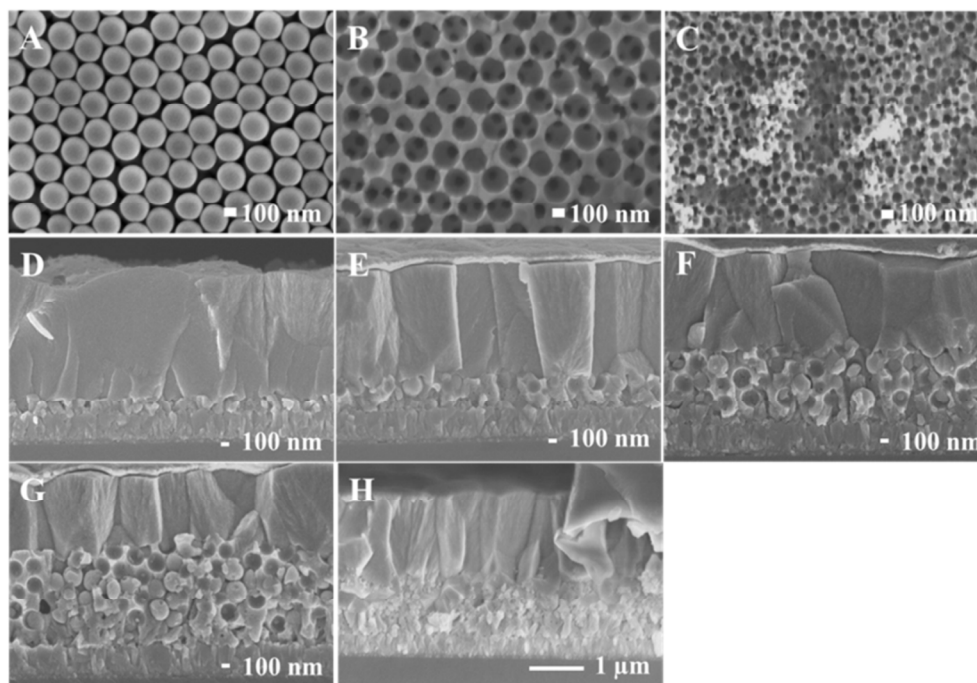


Figure 1. Top morphology images of 300 nm PC template (A) with P300 (B) and P100 (C) together with the cross section images of P (D), 300IO1 (E), 300IO3 (F), 300IO5 (G), and 100IO9 (H).

This paper will elaborate the consequences of incorporating ZnO IO structure in the $\text{Cu}_2\text{O}/\text{ZnO}$ solar cell. ZnO IO structures were fabricated by electrodeposition of ZnO inside a spin coated polystyrene spheres template. After removal of polystyrene spheres, Cu_2O was electrodeposited inside the ZnO IO matrix to form nanostructured solar cells. The effect of ZnO IO structure diameter and thickness on device performance was studied in-depth by comparing optical simulations performed using finite difference time domain (FDTD) protocols against experimental data. The IO structure could change the photon propagation direction such that more photon absorption occurs at the interface. Finally, this approach could be applied to other thin film solar cells where there is a mismatch between the charge collection length and the optical depth.

B. Experimental methods

ZnO planar films (~200nm) was grown on fluorine doped tin oxide coated glass (FTO, TEC 15) by electrodeposition in 0.05M $\text{Zn}(\text{NO}_3)_2 \cdot 6\text{H}_2\text{O}$ at -0.8V vs Ag/AgCl for 10 minutes. A potentiostat was used to supply constant potential during the deposition at 70°C. To fabricate face centered cubic (FCC) colloidal PC template, an aqueous suspension of polystyrene spheres (diameter of 300nm and 100nm) was spin coated on the ZnO planar film. The template was dried at 70°C for 15 minutes and then filled with ZnO which was grown by electrodeposition in 0.05M $\text{Zn}(\text{NO}_3)_2 \cdot 6\text{H}_2\text{O}$ at -0.9V versus Ag/AgCl for 5, 7.5, and 10 minutes. The PC template was removed by firing at 500°C for 1 hour. The Cu_2O layer was deposited by electrodeposition in 0.4 M CuSO_4 and 3 M lactic acid bath solution at 30°C. The pH of the solution was adjusted to 12.5 with NaOH. The depositions were done at -0.45V vs Ag/AgCl for a total charge of 1C cm^{-2} . Top electrodes were deposited by thermal evaporation of gold (approximately 100nm).

Current density – voltage (J-V) curves were measured using a SourceMeter with solar simulator (AM 1.5G, XEC-301S) while IPCE was measured in DC mode using PVE300 (Bentham). To minimize the contribution from the edges, black mask was used during J-V measurement. Diffuse transmittance measurements were performed with an integrating sphere (ISR-3100) using Shimadzu UV-3600 spectrophotometer. Cross sectional and morphological imaging was done using field emission scanning electron microscopy (FESEM, JEOL JSM-7600F). Electrochemical impedance measurements were performed with AutoLab PGSTAT302N instrument in combination with FRA2 module under AM1.5G illumination at open circuit conditions. Single sine 10 mV AC voltage waves were applied with frequency ranges from 1 MHz to 1000 Hz.

C. Results and discussion

The morphological images (**Figure 1a**) show that there is a successful self-assembly of 3D FCC polystyrene PC template and the subsequent infiltration with ZnO via electrodeposition. After firing, the PC templates are completely removed and the IO structures revealed. ZnO IO structures grown from 300nm and 100nm polystyrene beads were called P300 and P100 respectively. From cross section images (**Figure 1b**), it can be concluded that IO layer thickness can be controlled by adjusting the ZnO electrodeposition time. Deposition time of 5, 7.5, and 10 minutes inside 300 nm polystyrene PC templates resulted in about 280nm, 770nm, and 1100nm thick P300 - corresponding to approximately 1, 3, and 5 IO layers respectively. Adjusting the ZnO electrodeposition time to 10 minutes inside 100nm polystyrene PC templates gave about 750nm thick P100, which corresponded to approximately 9 IO layers. Devices made with 1, 3, and 5 layers of P300 were called 300IO1, 300IO3, and 300IO5 respectively while devices with 9 layers of P100 were called 100IO9. The crystallinity of ZnO IO structures were characterized and revealed a similar

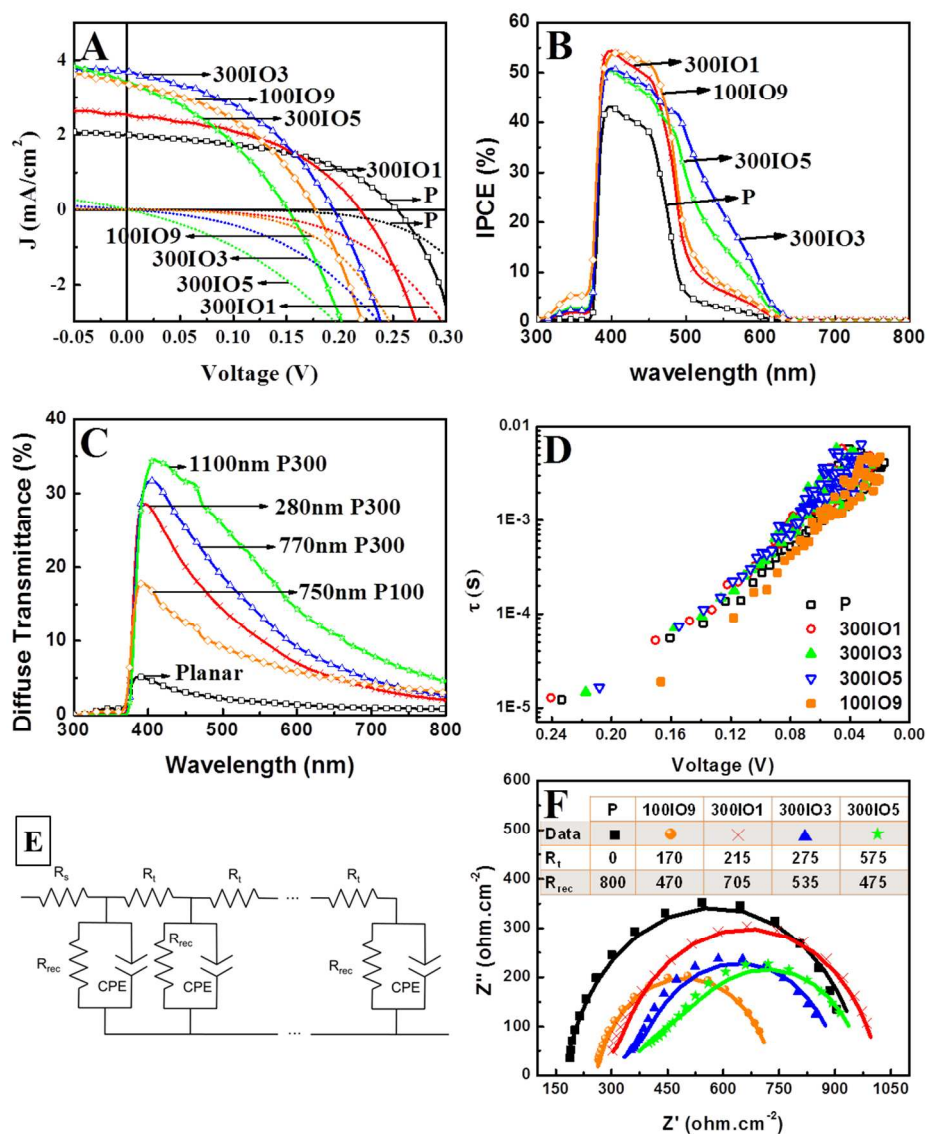


Figure 2. J-V characteristics (A) in light and dark together with the IPCE spectra (B), the ZnO diffuse transmittance (C) and minority carrier lifetime derived from photo voltage decay measurement (D) of samples. Complete equivalent circuit (E) employed to analyze the Nyquist plots obtained for planar and IO devices (F). The solid lines correspond to the fitting.

crystal structure (i.e. P63mc space group with hexagonal crystal structure) with the planar ZnO (Figure S1 in supplementary information). As similar deposition methods were employed, relatively comparable crystal structure of ZnO was explained. **Figure 1b** also shows spherical Cu_2O structures indicating successful Cu_2O infiltration within the IO layer despite the high pH of Cu_2O deposition condition which could damage the ZnO IO structure. The IO pore diameters and the distances between the centers of the pores were in agreement with the polystyrene beads size used. A continuous Cu_2O overlayer was grown on the IO structure to prevent electrical shunting between ZnO and gold electrodes.

J-V characteristics of various devices under AM1.5G illumination are reported in **Figure 2a** and the devices performances are presented in **Table 1**. Planar ZnO- Cu_2O devices reach PCE of 0.24%. Introduction of IO increases the J_{sc} of the devices. Among devices that employed P300, the J_{sc} of IO structured devices are enhanced with increasing number

of IO layers until it saturates at 3 IO layers, leading to higher PCEs. However, additional IO layers reduce its open circuit voltage (V_{oc}) and fill factor (FF). The best performing devices was 300IO3 with an efficiency of 0.29%. Due to similarity on the ZnO nanostructured thickness used, 300IO3 was compared against 100IO9 to gain knowledge on the effect of IO pore diameter on overall devices performances, which showed that 300IO3 has superior J_{sc} than 100IO9.

Table 1. Summary of power conversion efficiency of devices with different IO diameter and thickness.

	PCE (%)	J_{sc} (mA/cm^2)	Integrated J_{sc} (mA/cm^2)	V_{oc} (V)	FF
P	0.24	2	1.9	0.25	0.47
300IO1	0.25	2.53	2.8	0.22	0.44
300IO3	0.29	3.69	4	0.19	0.41
300IO5	0.18	3.41	3.5	0.15	0.35
100IO9	0.24	3.38	3.1	0.18	0.41

The origin of the reduction in V_{oc} and FF can be gleaned by the examination of the dark J-V characteristics. Dark J-V characteristics of devices (**Figure 2a**) shows that the current at positive voltage bias where electrons flow from ZnO to Cu_2O (dark cathodic recombination currents) are higher for IO devices against the planar one. These dark cathodic recombination currents are indicative of high recombination at the heterojunction interface which may cause reduction in both V_{oc} and FF²⁹. As the inverse opal did not prevent the formation of full depletion thickness within the 300 nm sphere (see supporting information), the V_{oc} reduction could be attributed to the other factors such as shifting on the ZnO Fermi energy level due to higher Cu_2O injection level or interfacial recombination increment caused by the interfacial area expansion^{18,30}. The photo voltage decay measurement was performed and carrier lifetime was extracted from the following equation³¹ and reported in **Figure 2D**.

$$\tau = - \frac{k T}{e} \left(\frac{dV_{oc}}{dt} \right)^{-1}$$

Where k , T , and e , t , and τ are Boltzmann's constant, absolute temperature, electron charge, time, and minority carrier lifetime respectively. Similar carrier lifetime was observed throughout the samples regardless of its interfacial area, suggesting that the recombination kinetics is dominated by the same process.

To further characterize the electrical processes in the devices, electrochemical impedance spectroscopy was performed under AM1.5G illumination at open circuit conditions. The Nyquist plots of all the devices with IO template (**Figure 2F**) consist of a straight 45° line at higher frequencies and a single arc at lower ones. The former represents the characteristic impedance fingerprint of a charge transport (R_t) process, whereas the latter corresponds to the chemical capacitance (CPE) in parallel to the recombination resistance (R_{rec})³². The transmission line model adopted to estimate the R_t and R_{rec} inside the devices is represented in **Figure 2E**. From the analysis of the results (**Figure 2F**), significantly smaller R_t is obtained when reducing the ZnO IO thickness for devices with 300 nm IO pore size, with the minimum one observed when 100 nm IO pore size is used. Remarkably, the transport resistance feature is not present in the planar devices spectrum, in agreement with the shorter path for the charge extraction. Hence, nanostructuring with IO geometry increases the transport resistance of the whole devices. The R_{rec} at open circuit conditions decreases with introduction of IO geometry. This signifies higher interfacial recombination on the devices with IO geometry, which is in agreement with the result from the dark J-V characteristic analysis. The V_{oc} of 300IO5 is smaller than V_{oc} of 300IO1, 300IO3, and 100IO9 due to its lowest R_{rec} and highest dark cathodic recombination currents. In addition, this device also presents the highest R_t . Therefore, due to higher recombination at ZnO/ Cu_2O interface as well as higher charge transport resistance, 300IO5 has the lowest performance compared to 300IO1, 300IO3, and 100IO9.

IPCE spectra (**Figure 2b**) reveal that the introduction of IO layers results in changes in IPCE. The integrated J_{sc} from IPCE was within 10 % error of the J_{sc} obtained from the J-V characteristic. When P300 was used, IPCE for $\lambda > 475$ nm was enhanced prominently as compared to devices with P100. Increasing the IO layer thickness increases the IPCE for $\lambda > 475$ nm until it saturates at 3 IO layer for devices that employed P300. The J_{sc} enhancement brought on by nanostructuring is often related to interfacial area, and improvement of the charge carrier collection as the electron transporting material (ZnO) penetrates inside the light absorbing Cu_2O layer^{17,18} allowing

the collection of photoelectrons excited deep within the Cu_2O . However, 300IO5 devices, which have a higher interfacial area and more extended ZnO layer than 300IO3 devices, display comparable IPCE with 300IO3 devices. It can be noted that for the same Cu_2O amount, the 300IO3 cell would have a thicker Cu_2O overlayer compared to 300IO5. To eliminate the effect of varying overlayer thicknesses, devices with similar overlayer thicknesses (~800 nm) were prepared. These devices also yielded the same trend (Figure S3 in supplementary information). Additionally, 300IO3 have a superior J_{sc} than 100IO9 though 100IO9 were expected to have higher J_{sc} than 300IO3 from interfacial area point of view. To understand these anomalies, both experimental and simulated optical measurements were carried out. Diffuse transmittance (which measures the intensity of light transmitted and scattered) of the ZnO layer alone (**Figure 2c**), reveal that IO structures increase the diffuse transmittances for $\lambda > 375$ nm. In P300 case, increasing P300 thickness enhances the diffuse transmittance with similar plateau being observed. In spite of similar ZnO nanostructure thickness, 9 layers of P100 have inferior diffuse transmittance than 3 layers of P300.

When photon encounters spheres with different refractive index material, it can be refracted and scattered. If the sphere is built from a good absorber material, the refracted photon would be absorbed immediately. However, when a weak absorbing material is used, the refracted photon could undergo an internal reflection or scattering. This phenomenon is governed by the photon energy, refractive index and extinction coefficient of the material, as well as the sphere diameters. To predict the photon density distribution within the ZnO/ Cu_2O devices, optical absorption simulation was performed using FDTD (Lumerical, Inc) in the device. The device is modeled as a 3-D geometry of FTO (500nm)/ZnO (200nm)/ Cu_2O infiltrated ZnO IO layer/ Cu_2O overlayer/Au (100nm). The IO pore diameter, distance between the centers of the pores, IO layer thickness, and Cu_2O overlayer thickness were adjusted according to **Figure 1b**. The IO structures are assumed to be in a perfect FCC configuration. To predict the effect of pore diameter on photon propagation within the film, the Cu_2O sphere diameter was varied from 100 nm to 400 nm while the number of IO layers was fixed to 5. The influence of the ZnO IO thickness was studied by tuning the number of IO layers while fixing the pore diameter at 300nm. The absorption enhancement was calculated by normalizing the absorption from FTO/ZnO/ Cu_2O infiltrated ZnO IO layer against a FTO/ZnO/ Cu_2O structure where the Cu_2O thickness is the same as the infiltrated thickness. This accounts for the total Cu_2O thickness increment with increasing the IO layers or diameter. Increasing the absorption enhancement here represents an increment of photocarrier generation close to the electron collector (i.e. ZnO).

The absorption enhancement for 5 IO layers for different IO pore diameter is calculated and reported in **Figure 3a**. As the optical depth of Cu_2O for $\lambda \leq 475$ nm is less than 100 nm³³, Cu_2O acted as an efficient absorber (the IO pore diameter used was ≥ 100 nm). Due to the weak absorption coefficient of Cu_2O at $\lambda > 475$ nm, the optical absorption enhancement for $\lambda > 475$ nm is critically dependent on the IO diameter. Only IO structures with a pore diameter of 200 nm and more demonstrate a significant enhancement of the film absorption for $\lambda > 475$ nm. However, there is no significant improvement observed within the pore diameter range of 200 nm to 400 nm.

Figure 3b shows that employing 3 layers of IO film and above increases the photon absorption throughout the entire spectrum.

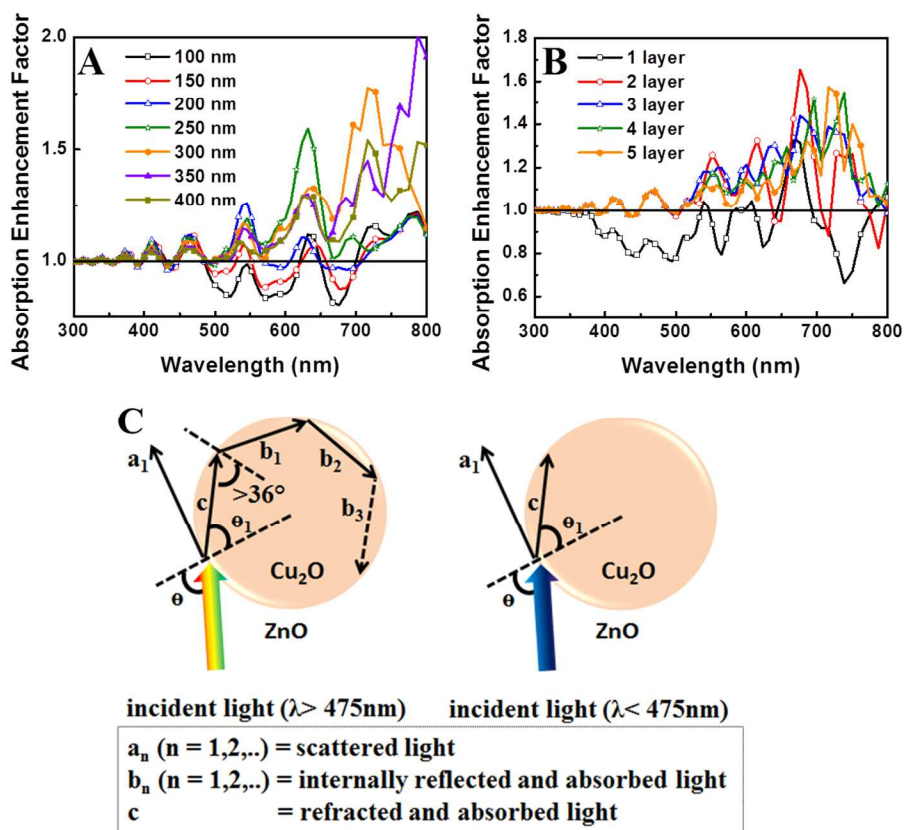


Figure 3. The calculated absorption enhancement factor for 5 IO layers with different IO pore diameter (A) and for 300 nm IO pores diameter with different IO layer thickness (B) together with the schematic diagram of light propagation inside Cu_2O sphere (C).

For 1 layer of IO, negative absorption enhancement is observed probably due to the smaller Cu_2O volume as compared to the Cu_2O thin film. The absorption enhancement is saturated at 3 IO layers with no significant absorption enhancement observed with increasing IO layers. In summary, only IO structures with diameter $> 200\text{nm}$ and thickness ≥ 3 IO layers are projected to increase the photo-carrier generation near ZnO for $\lambda > 475\text{nm}$. To understand the photon propagation behavior inside the films, the absorption cross sections were simulated by calculating the power absorption per unit volume (P_{abs}). From the simulated absorption cross sections (Figure 4), it was shown that Cu_2O infiltrated IO layers were indeed successfully acting as a scattering center. For 100IO9, photon with $\lambda \leq 475\text{nm}$ are strongly scattered while no significant scattering is observed for photon with $\lambda > 475\text{nm}$. Increasing the IO diameter to 300 nm changes the absorption cross section tremendously. Cu_2O infiltrated P300 is a strong scattering center for photons with $\lambda \leq 475\text{nm}$ while relatively weak scattering is observed at $\lambda > 475\text{nm}$. Due to the dimension and refractive index different between ZnO and Cu_2O , the curvature of the 1st Cu_2O infiltrated IO layer acts as a photon concentrator for the region where the photon is strongly scattered (at $\lambda \leq 475\text{nm}$). According to Snell's law, a critical angle of 36° was observed at ZnO/ Cu_2O interface at $\lambda = 500\text{nm}$. In the weak scattering region, the curvature of 2nd Cu_2O infiltrated IO layer and above could act as a back reflector for the photons, allowing an internal reflection to occur. Due to photon scattering and Cu_2O absorption, majority of the photons are completely absorbed by the end of the 3rd Cu_2O infiltrated IO

layers. Therefore, additional IO thickness beyond 3 layers does not significantly enhance its absorption, confirming the calculated absorption enhancement result.

For devices that employ P300, due to strong scattering at $\lambda \leq 475\text{nm}$, the photo-carrier generation is closer towards the electron collector region than planar devices. The electron collection efficiency is foreseen to be higher when photo-generated electron-hole pairs are located near the interface, as the distance for electrons to drift before they are collected by ZnO is smaller. This explains the superior IPCE for devices that employ P300 at $\lambda \leq 475\text{nm}$. Due to weak scattering effect at $\lambda > 475\text{nm}$, the photo-carrier generation region are wider. Longer wavelength creates wider carrier-generation region. Hence, the IPCE degrades significantly at $\lambda > 475\text{nm}$ due to longer distance for electron drift before they are collected by ZnO.

Though 300IO5 had more extended junction, higher diffuse transmittance, and at least 2.5 times higher interfacial area than 300IO3, 300IO5 had slightly smaller J_{sc} value than 300IO3. This behavior matches well with the simulated absorption enhancement and absorption cross section profile of both 3 and 5 layers of Cu_2O incorporated P300. As almost all photons that pass through the Cu_2O infiltrated P300 would be absorbed by the first 3 IO layers, increasing the IO layer above 3 layers does not increase the J_{sc} . Additionally, the 2 layers above the first 3 IO layers would act as additional interfacial area that could lead to additional interfacial recombination. Furthermore, larger R_t could be observed from the impedance measurement due to thicker ZnO film without significant absorption enhancement. Therefore, 300IO3 has the highest J_{sc} because its structure

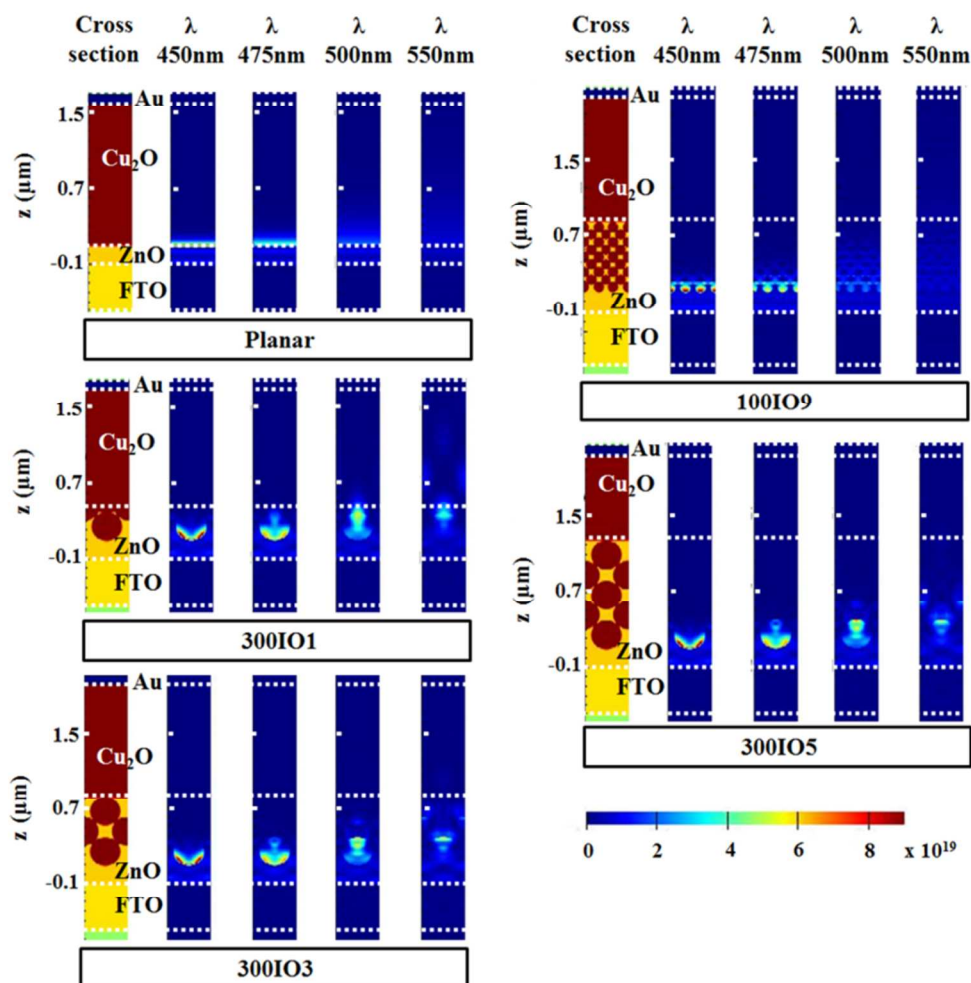


Figure 4. The simulated P_{abs} of devices with different IO diameter and thickness.

provides the highest absorption enhancement with minimum R_t . Hence, a slight reduction in the J_{sc} is expected from the 5 layer Cu_2O incorporated P300 structures due to the increased interfacial recombination (and no improved optical absorption). In conclusion, fine tuning the IO layer thickness that could maximize absorption enhancement while minimizing the interfacial area enhancement would be ideal for $\text{ZnO}/\text{Cu}_2\text{O}$ system. It was found that 3 layers of IO layers were adequate to fully enhance the absorption from both theoretical and experimental point of view.

The superior J_{sc} value of 300IO3 against 100IO9 despite its lower interfacial area could be explained by the strong scattering effect of Cu_2O incorporated P300 at $\lambda > 475$ nm. It was simulated previously that only IOs with diameter greater than 200 nm was able to scatter photons with $\lambda > 475$ nm. In addition, from the diffuse transmittance, it was shown that P300 had a higher scattering efficiency than P100. Hence, the results were in agreement with the simulation data that IO > 200 nm could scatter light at $\lambda > 475$ nm which could not be done by IO with diameter < 200 nm.

Conclusions

This study elaborated the significance of photon management on improving the photocurrent of $\text{ZnO}/\text{Cu}_2\text{O}$ solar cell. By amplifying the photon absorption at the interface, the IPCE of

the devices can be enhanced resulting in J_{sc} increment. As IO structures introduce more interfacial area, reductions of V_{oc} and FF occur due to higher interfacial recombination. Although the increased interfacial area could increase the electron collection efficiency, employing suitable IO geometry is crucial to amplify the photon absorption near the interface. From the experimental data correlated with FDTD simulation, it is clear that the introduction of IO structures with pore diameter > 200 nm and thickness ≥ 3 layers inside $\text{ZnO}/\text{Cu}_2\text{O}$ solar cell could enhance the IPCE value especially for $\lambda > 475$ nm. The simulation supports the hypothesis that IO not only increases the IPCE due to the extension of ZnO into the Cu_2O films, but also the magnification of photon absorption near the interface. Although more effort should be done to improve the overall device performances, this study explores an approach to device architectures that would improve the photocurrent densities by focusing the photon absorption near the $\text{ZnO}/\text{Cu}_2\text{O}$ junction to increase the charge collection efficiency. This study opens the possibility of applying IO structures on other thin film solar cells that suffers from a mismatch between the optical depth and carrier collection length.

Acknowledgements

The authors gratefully acknowledge Prof. Subodh Mhaisalkar for fruitful discussions. The authors also thank the Singapore-

Berkeley Research Initiative for Sustainable Energy (SinBeRISE) CREATE programme and NTU-A*STAR Silicon Technologies Centre of Excellence under the program grant No. 112 3510 0003 for funding.

Notes and references

^a School of Materials Science and Engineering, Nanyang Technological University, 50 Nanyang Avenue, Singapore 639798. Email: Nripan@ntu.edu.sg

^b Energy Research Institute@NTU (ERI@N), Research TechnoPlaza, X-Frontier Block, Level 5, 50 Nanyang Drive, Singapore 637553.

- 1 N. Yantara, Y. Fang, S. Chen, H. A. Dewi, P. P. Boix, S. G. Mhaisalkar and N. Mathews, *Chem. Mater.*, 2015, **27**, 2309.
- 2 S. Dharani, H. K. Mulmudi, N. Yantara, P. T. Thu Trang, N. G. Park, M. Graetzel, S. Mhaisalkar, N. Mathews and P. P. Boix, *Nanoscale*, 2014, **6**, 1675–9.
- 3 Y. S. Lee, D. Chua, R. E. Brandt, S. C. Siah, J. V Li, J. P. Mailoa, S. W. Lee, R. G. Gordon and T. Buonassisi, *Adv. Mater.*, 2014, **26**, 4704–4710.
- 4 T. Shinagawa, K. Shibata, O. Shimomura, M. Chigane, R. Nomura and M. Izaki, *J. Mater. Chem. C*, 2014, **2**, 2908.
- 5 T. Minami, Y. Nishi and T. Miyata, *Appl. Phys. Express*, 2013, **6**, 044101.
- 6 H. Raebiger, S. Lany and A. Zunger, *Phys. Rev. B*, 2007, **76**, 1–5.
- 7 J. J. Lofeski, *J. Appl. Phys.*, 1956, **27**, 777–784.
- 8 T. Minami, Y. Nishi and T. Miyata, *Appl. Phys. Express*, 2015, **8**, 022301.
- 9 A. E. Rakhshani, A. A. Al-Jassar and J. Varghese, *Thin Solid Films*, 1987, **148**, 191–201.
- 10 S. Bijani, L. Martinez, M. Gabas, E. A. Dalchiale and J.-R. Ramos-Barrado, *J. Phys. Chem. C*, 2009, **113**, 19482–19487.
- 11 T. D. Golden, M. G. Shumsky, Y. Zhou, R. A. VanderWerf, R. A. Van Leeuwen and J. A. Switzer, *Chem. Mater.*, 1996, **8**, 2499–2504.
- 12 K. Han and M. Tao, *Sol. Energy Mater. Sol. Cells*, 2009, **93**, 153–157.
- 13 L. Wang, N. Detacconi, C. Chenthamarakshan, K. Rajeshwar and M. Tao, *Thin Solid Films*, 2007, **515**, 3090–3095.
- 14 Y. S. Lee, J. Heo, S. C. Siah, J. P. Mailoa, R. E. Brandt, S. B. Kim, R. G. Gordon and T. Buonassisi, *Energy Environ. Sci.*, 2013, **6**, 2112.
- 15 K. P. Musselman, Y. Ievskaya and J. L. MacManus-Driscoll, *Appl. Phys. Lett.*, 2012, **101**, 253503.
- 16 J. Cui and U. J. Gibson, *J. Phys. Chem. C*, 2010, **114**, 6408–6412.
- 17 K. P. Musselman, A. Wisnet, D. C. Iza, H. C. Hesse, C. Scheu, J. L. MacManus-Driscoll and L. Schmidt-Mende, *Adv. Mater.*, 2010, **22**, E254–8.
- 18 N. Yantara, N. Mathews, K. B. Jinesh, H. Kumar and S. G. Mhaisalkar, *Electrochim. Acta*, 2012, **85**, 486–491.
- 19 T. Gershon, K. P. Musselman, A. Marin, R. H. Friend and J. L. MacManus-Driscoll, *Sol. Energy Mater. Sol. Cells*, 2012, **96**, 148–154.
- 20 L. J. Diguna, Q. Shen, J. Kobayashi and T. Toyoda, *Appl. Phys. Lett.*, 2007, **91**, 023116.
- 21 A. Mihi, M. E. Calvo, J. A. Anta and H. Miguez, *J. Phys. Chem. C Lett.*, 2008, **112**, 13–17.
- 22 S. Nishimura, N. Abrams, B. a Lewis, L. I. Halaoui, T. E. Mallouk, K. D. Benkstein, J. van de Lagemaat and A. J. Frank, *J. Am. Chem. Soc.*, 2003, **125**, 6306–10.
- 23 J.-H. Shin, J.-H. Kang, W.-M. Jin, J. H. Park, Y.-S. Cho and J. H. Moon, *Langmuir*, 2011, **27**, 856–60.
- 24 A. Stein, B. E. Wilson and S. G. Rudisill, *Chem. Soc. Rev.*, 2013, **42**, 2763–803.
- 25 M. Wang and X. Wang, *Sol. Energy Mater. Sol. Cells*, 2008, **92**, 357–362.

- 26 J. Kim, H. S. Kim, J. H. Choi, H. Jeon, Y. Yoon, J. Liu, J. Park and P. V Braun, 2014.
- 27 L. Kong, Q. Dai, C. Miao, L. Xu and H. Song, *J. Colloid Interface Sci.*, 2015, **450**, 196–201.
- 28 Y. Chen, H. Yan, B. Yang, Y. Lv, M. Wen, J. Xu, M. Wu, X. Zhu and Z. Fu, *Appl. Phys. A*, 2009, **98**, 467–472.
- 29 B. Rand, D. Burk and S. Forrest, *Phys. Rev. B*, 2007, **75**, 115327.
- 30 D. Kieven, T. Dittrich, A. Belaidi, J. Tornow, K. Schwarzburg, N. Allsop and M. Lux-Steiner, *Appl. Phys. Lett.*, 2008, **92**, 153107.
- 31 J. E. Mahan, T. W. Ekstedt, R. I. Frank and R. Kaplow, *IEEE Trans. Electron Devices*, 1979, **26**, 733.
- 32 J. Bisquert, M. Grätzel, Q. Wang and F. Fabregat-Santiago, *J. Phys. Chem. B*, 2006, **110**, 11284–11290.
- 33 C. Malerba, F. Biccari, C. Leonor Azanza Ricardo, M. D’Incau, P. Scardi and A. Mittiga, *Sol. Energy Mater. Sol. Cells*, 2011, **95**, 2848–2854.